Bulletin of the Seismological Society of America. Vol. 66, No. 4, pp. 1111–1120. August 1976

FOCAL MECHANISM OF THE AUGUST 1, 1975 OROVILLE EARTHQUAKE

By Charles A. Langston and Rhett Butler

ABSTRACT

Long-period teleseismic *P* and *S* waves from the WWSS and Canadian networks are modeled to determine the focal parameters for the main shock in the Oroville earthquake series. Using the techniques of *P* first motions, wave-form synthesis, and phase identification, the focal parameters are determined as follows: dip 65°; rake −70°; strike 180°; depth 5.5 ± 1.5 km; moment 5.7 ± 2.0 × 10^{24} dyne-cm; and a symmetric triangular time function 3 sec in duration. This is a north-south striking, westward dipping, normal fault with a small component of left-lateral motion. The time separation between the small foreshock and mainshock appears to be 6.5 sec at teleseismic distances, rather than 8.1 sec as observed at short distances.

Introduction

Although the mainshock in the Oroville earthquake sequence was relatively small by seismological standards ($M_L = 5.7$), the interest in this event is enhanced by the possible relation it has with the nearby Oroville Reservoir. The obvious scientific and legal ramifications of induced seismicity has made this particular field currently one of the fastest growing and most exciting areas of geophysics. It is not the object of this paper, however, to speculate on any causal relationship of the earthquakes to the reservoir. Instead, we will present results for the focal parameters of the mainshock of August 1, 1975, in light of some recently presented techniques of wave-form analysis.

The main Oroville shock had some peculiarities which effectively thwarted standard location and focal mechanism techniques using nearby stations. As reported by Morrison *et al.* (1975), a magnitude 4.5 foreshock preceded the mainshock by 8.1 sec. Consequentially, the location of the mainshock, although inferred to be at the same place as the foreshock, was hard to pin down. The foreshock was also large enough to obscure local *P* first motions, so that the faulting mechanism was also unknown until sufficient aftershock data were processed to get an indirect look at the fault plane (Bufe *et al.*, 1976; Ryall and VanWormer, 1975). Because of these reasons, and also since the event was well recorded at teleseismic ranges, a body wave-form analysis was carried out to determine estimates of the orientation, depth, time function, and seismic moment parameters for the earthquake.

Data and Analysis

Immediately after the earthquake, requests for the long- and short-period vertical components from each station in the WWSS and Canadian networks were sent out with excellent response from most. This particular component was requested primarily because of a travel-time study being conducted for the region. Fortunately, in view of the clear long-period *P* and *S* waves observed, some stations sent the horizontal components also. These turned out to be very helpful in constraining the focal mechanism.

Before any wave-form interpretation could be done, however, the extent of interference of the foreshock with the mainshock had to be determined. Figure 1 shows the short-period vertical component for the station MSO. This is one of the few teleseismic stations

where the foreshock is clearly recorded, and only because MSO is relatively close to the epicenter. The long-period component shows little interference between the shocks at this particular distance. For more distant stations, the foreshock is virtually always in the noise, even on the short-period components. Figure 1 also indicates a possible discrepancy in the time between the foreshock and mainshock. Where the foreshock and the *P* wave for the mainshock can be read on short-period seismograms, the time difference observed is nearer 6.5 sec than the 8.1 sec reported by Morrison *et al.* (1975) from local stations. An explanation for this possible discrepancy based on the focal mechanism will be given in the discussion.

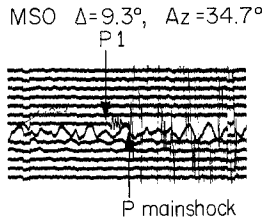

FIG. 1. Copy of the short-period vertical component at MSO showing the foreshock and mainshock *P* arrivals.

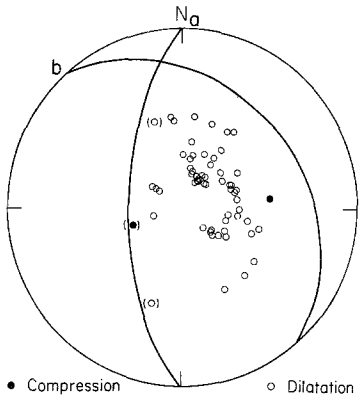

Plane "a": δ=65°, λ=-70°, θ=180°
Plane "b": δ=32°, λ=-110°, θ=319°

FIG. 2. Equal-area projection of the lower half of the focal sphere showing the *P* first motions. The brackets indicate questionable readings.

Focal parameters for the main event were determined by a multi-stage process; each stage representing an increase in resolution for some particular set of parameters or some individual parameter.

Figure 2 shows the distribution of *P*-wave first motions on an equal area projection of the lower half of the focal sphere. Table 1 cites the stations used in this study. Basically, the first motions indicate normal faulting but the various orientation angles are unconstrained by $\pm 30°$ or more. In order to constrain the orientation and also determine the depth, time function, and moment, long-period *P* waves were examined at ranges greater than 30° but less than 90° to avoid upper mantle and core structural complications. By modeling the *P* wave form in the time domain, source information can be extracted by examining the timing, shape, and relative amplitudes of the phases *P*, *pP*, and *sP*, assuming that the local source crustal structure is known. The computational techniques and conventions are described in detail by Langston and Helmberger (1975) and by Helmberger (1974) and will only be touched upon.

TABLE 1

WWSSN AND CANADIAN STATIONS USED IN THIS STUDY

Station	$\Delta^{(\circ)}$	$Az^{(\circ)}$	*P* First Motion*	Moment ($\times 10^{-24}$ dyne-cm)
ALE	47.20	8.9	D	5.0
BLC	29.08	22.8	D	
EDM	14.88	19.6	D	
FBC	39.33	34.2	D	4.6
FCC	26.11	33.2	D	
FFC	20.18	34.4	D	
FSJ	15.09	354.0	D	
MBC	36.90	0.9	D	
MNT	35.48	64.2	D	3.9
OTT	34.02	64.7	D	3.2
PHC	11.98	341.8	(D)	
PNT	9.97	7.6	D	
RES	37.44	11.3	D	
SCH	39.26	48.4	D	7.4
SES	13.26	30.9	D	
STJ	49.1	56.7	D	6.5
VIC	9.16	352.4	D	
YKC	23.46	8.3	D	
LHC	24.79	58.2	D	
INK	24.92	347.2	D	
AAM	28.67	71.9	D	
ANP	92.84	306.0	D	
AQU	88.93	31.6	D	
ARE	72.64	129.5	D	8.0
ATU	96.64	26.9	D	
BHP	48.23	117.5	D	4.6
BKS	1.65	198.1	(D)	
BLA	32.18	80.7	D	3.0
BOG	55.12	116.3	D	
CAR	56.28	105.3	D	
COP	77.49	24.7	D	
DAL	21.06	100.5	D	
ESK	72.01	31.9	D	
GOL	12.53	83.7	C	
GSC	5.63	135.9	D	
HNR	87.14	255.4	D	
JCT	19.94	110.0	D	
KEV	68.70	11.2	D	
KIP	35.88	250.7	(C) reported	
LPB	74.75	127.0	D	5.5
LPS	37.93	122.2	D	
LUB	16.89	104.2	D	
MAT	74.65	304.7	D	7.1
MSO	9.25	34.7	D	
NNA	65.96	131.0	D	6.7
NUR	76.62	16.4	D	
OXF	26.10	90.7	D	
PTO	79.27	45.0	D	
SCP	33.20	73.4	D	
SHA	28.61	97.4	D	
SHK	79.41	306.0	D	11.0
SJG	52.18	97.4	D	6.0
STU	82.00	30.3	D	

Continued

TABLE 1—*Continued*

Station	$\Delta^{(\circ)}$	$Az^{(\circ)}$	*P* First Motion*	Moment ($\times 10^{-24}$ dyne-cm)
TOL	82.61	43.5	D	6.2
TRI	86.30	29.6	D	
TUC	11.29	125.8	D	
UME	72.72	16.7	D	
VAL	71.19	37.5	D	
WES	37.66	68.9	D	3.1
PAS	5.96	151.5	D	
				av. = 5.7
				σ = 2.0

*C = compression; D = dilatation.

A synthetic seismogram is computed by first calculating the sum of ray responses for an imbedded point dislocation, of some orientation and depth, in a layered elastic medium. An area normalized dislocation time function is assumed and the displacement seismogram convolved with a Q operator (Futterman, 1962; Carpenter, 1966) and the 15- to 100-instrument impulse response to produce the final synthetic. This is then compared directly with the observation. The far-field time function assumed in this study is a simple triangular pulse parameterized by the rise and fall-off times (δt_1 and δt_2). The T/Q parameters (T= travel time in sec) assumed are 1.0 and 4.0 for P and S waves, respectively. Comparison between the observed seismogram and synthetic is done by trial-and-error and by a formal generalized inverse (Mellman *et al.*, 1975). The particulars of this generalized inverse are described in detail by Langston (1976).

The P wave forms chosen for study were processed in the manner described by Langston (1976). Eighteen long-period P waves were used and are shown as the *top* seismograms, at each station, in Figure 3. This station distribution represents the best azimuthal variation possible with the long-period data set. Pacific azimuths are not included because of very poor signal quality and the scarcity of stations at those azimuths and the specified range interval. The wave forms exhibited in Figure 3 are very simple in character. Distortion due to the instrument response is relatively minor for these particular seismograms so it is easy to identify the polarities of the major arrivals. Every station shows a dilatational first arrival with a major compression directly behind it. Examining the strength and polarity of the radiation pattern from a shallow, normal dip-slip, point dislocation in a typical continental crust predicts that the combined phases of pP and sP should be compressional and larger than the dilatation P wave at teleseismic distances. Using this hypothesis several models were constructed with very satisfactory results. The crustal model assumed in this procedure is taken from Eaton (1966) and is displayed in Table 2.

Good fits to the P waves were obtained by using a point dislocation source model at a depth of 5 km, dip of 65°W, and with a symmetric triangular time function 3 sec in duration. The depth is controlled by the interference of P and pP and the dip by their amplitude ratios. It was quickly apparent, however, that the strike and rake of the fault plane remained unconstrained to the same degree as found by the first-motion study. An inversion was attempted to see if the small differences these parameters should produce in the data set were resolvable, but results were negative. The starting model turned out to be the best model with the "resolution" matrix indicating that the strike and rake were very poorly constrained.

In an effort to constrain these parameters the few *S* waves were examined. The horizontal components were digitized and then rotated into the ray azimuth; data are shown in the *left* half of Figure 4. This particular *S*-wave data set exhibits problems characteristic of most *S* wave forms. SJG shows some long-period noise ($T \sim 60$ sec) and a relatively small signal. However, since a rotation is insensitive to base-line shifts when

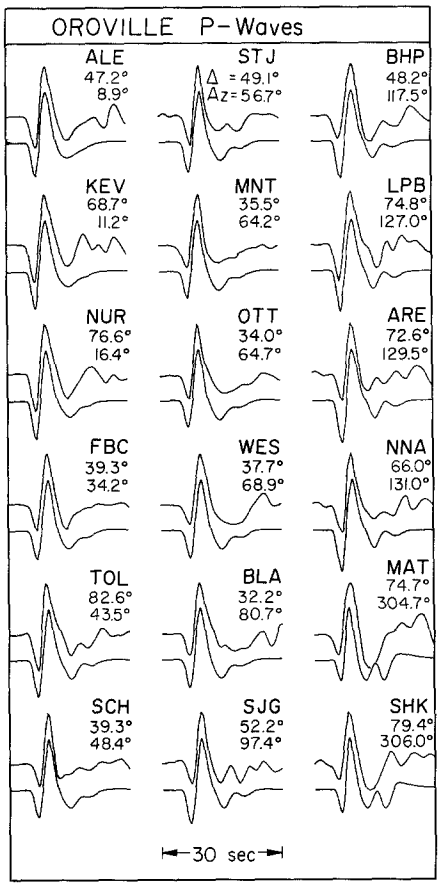

FIG. 3. Observed and synthetic long-period wave forms for the 18 stations used. Each seismogram pair consists of the observed on top and computed directly below for each station.

TABLE 2

CRUST MODEL

α (km/sec)	β (km/sec)	ρ (gm/cm^3)	Th (km)
6.0	3.5	2.7	10.0
6.8	3.9	2.8	10.0
8.0	4.6	3.3	—

relative wave shapes are considered, long-period drift should contribute very little error in the rotation. MAT and TRI exhibit complicated arrivals after the first 10 sec which are, presumably, core phases and *S*-coupled P_L waves (Helmberger and Engen, 1974). Of the four, NNA would appear to represent the best rotated seismograms, due to ideal range, good back azimuth, and high amplitude *SH*. Despite these problems, valuable

information about the source is present in the first 10 sec, contained in the interference of S and sS. Since the source is very shallow, as determined by the P waves, a strict use of the standard techniques for determining S polarization angles would be misleading and erroneous due to this interference. An approach of modeling directly the SV and SH components was therefore taken.

The comparison between observed and synthetic was done by trial and error with the employment of a special metric to compare wave shapes and amplitudes in a more quantitative sense. Consider the scheme illustrated in Figure 5. Define an "effective" polarization angle by simply considering the inverse tangent of the magnitude of the SV/SH amplitude ratio, or

$$\gamma_i = \tan^{-1}(|A_{SV}/A_{SH}|) \tag{1}$$

where γ_i is the "effective" polarization at the ith station. This relation measures the

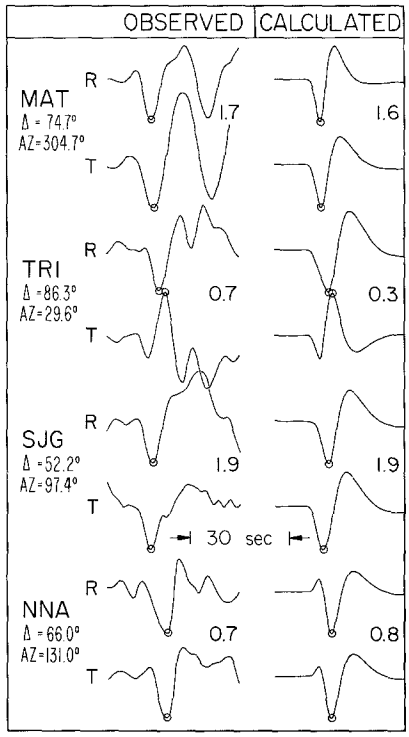

FIG. 4. Observed and synthetic SV and SH at four stations. The *left-hand* column contains the observed rotated S waves and the *right*, the corresponding synthetics for the final model. R and T stand for the radial and tangential components, respectively. The numbers in the right center of each pair correspond to the SV/SH amplitude ratio at the points indicated by the small circles.

effective strength of the two shear components. To measure wave shape and polarities define another angle, ω_k, by

$$\omega_k = \tan^{-1}(A_1/A_2), k = 1, 2 (SV \text{or } SH). \tag{2}$$

These relations assume that the approximate time of sS is known so that an appropriate time interval can be considered and the arrivals identified. In relation (2), if the seismogram has only one peak within the time interval, it is designated with A_2 and A_1 set to zero. This insures stability in ω_k if the direct S wave goes through a node while sS stays

relatively constant in amplitude. Using relations (1) and (2), further define a residual function or norm, ξ^2, by

$$\xi^2 = \sum_{i=1}^{n} \left\{ (\gamma_i - \bar{\gamma}_i)^2 + \sum_{k=1}^{2} (\omega_k - \bar{\omega}_k)_i^2 \right\} \tag{3}$$

where,

i = index of the ith station
$k = 1$, SV; 2, SH at the ith station
$-$ = theoretical value of the particular angle.

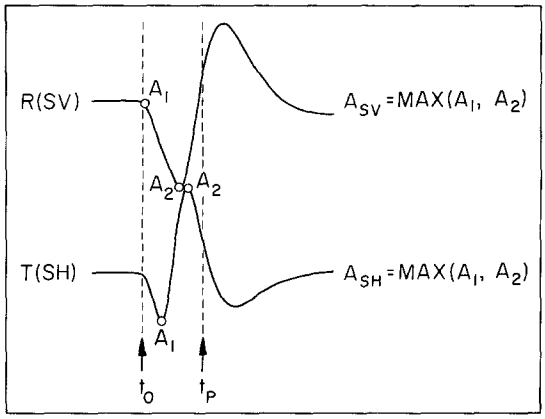

FIG. 5. Scheme for parameterizing *SV-SH* wave-form pairs.

TABLE 3

THE RESIDUAL FUNCTION, ξ, VERSUS VARIOUS ORIENTATION ANGLES FOR THE OROVILLE *S*-WAVE DATA

λ (deg)	θ (deg)	ξ
−80	170	0.391
−80	180	0.416
−80	190	0.589
−70	170	0.386
−70	180	0.338
−70	190	0.508
−60	170	0.587
−60	180	0.506
−60	190	0.790

*λ = rake, θ = strike, and $\delta = 65°$.

Using the values found by the *P*-wave modeling for depth, dip, and time function, the rake (λ) and strike (θ) were varied in 10° increments over several classes of models, e.g., right-lateral and left-lateral orientations. To fit the polarities and wave shapes it was apparent that a left-lateral model had to be used. Table 3 illustrates the value of ξ versus various orientations around the orientation of rake −70° and strike 180° which produced the minimum value of ξ. These values indicate that trade offs occur in λ and θ which could possibly allow the rake to be in the interval −70° to −80° and the strike within 170° to 180°. No weighting functions were applied to (3) and the statistics of such a parameterization were not investigated. However, high values of ξ, e.g., 0.4, clearly

represent bad fits as determined by simple visual correlation of the sizes and timing of observed peaks. It therefore serves as a good quantitative indicator to be used in conjunction with seismogram overlays. The *right* side of Figure 4 shows the final *S*-wave synthetics for the four stations used. The *SV* waves (*R*) contain the phases *S*, *pS*, and *sS*. The *SH* waves (*T*) contain only *S* and *sS*. Amplitudes are scaled by the receiver function for an upper crust of compressional and shear-wave velocity 6.0 and 3.5 km/sec, respectively. Most seismograms show *S* and *sS* to be in phase except for *TRI*(*SH*) and *NNA*(*SV* and *SH*) where they are opposite polarity.

An independent check on the depth was performed by reading *P*-wave arrivals on the short-period vertical seismograms. Figure 6 shows a histogram of the number of arrival-time picks versus time relative to the direct *P* wave, for the available teleseismic stations. Arrival times were placed in 0.1-sec cells on each side of the time read, the estimated reading error being ± 0.1 sec. This effectively spreads the arrival over 0.2 sec. Hence, the histogram shows twice the actual number of readings. A distinct bimodal distribution emerged from this process with peak times at about 1.6 and 2.5 sec. Because the long-

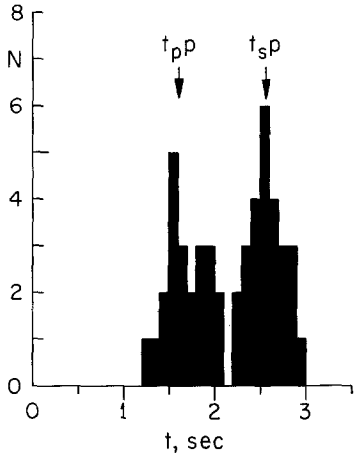

FIG. 6. Histogram of arrival time versus number of picks showing the bimodal distribution attributed to *pP* and *sP*.

period *P* waves yielded a depth of approximately 5 km, these arrivals are interpreted to be the phases *pP* and *sP*. These times yield depths of 5.1 and 5.7 km from the respective phases. A maximum error of 0.4 sec, based on the widths of the distributions, yields an average depth of 5.5 ± 1.5 km.

The final *P*-wave model comparisons are shown in Figure 3. These synthetics contain 20 crustal rays with arrival times up to about 20 sec after the first *P* arrival. In general, the fits are satisfactory. The model predicts a dilatational direct *P* with an immediate compressional arrival composed of *pP* and *sP*. The small arrivals after these major phases are essentially interference effects produced by the addition of many small crustal reverberations adding in phase at these wavelengths. This particular effect can explain the start of the *P* coda for all the stations except MAT and SHK where the model predicts an unobserved arrival. This is not too disconcerting since these interference effects are dependent, to a large degree, on the exact nature of the source crust. This does imply, however, that, given the particular orientation and depth, the crustal structure at Oroville changes laterally, either in velocity/thickness or in the sharpness of layer boundaries.

Scaling the synthetic wave forms directly to the observations gives a moment of $5.7 \pm 2.0 \times 10^{24}$ dyne-cm (Table 1). The error is one standard deviation in the amplitude scatter.

Superimposed on this error is a possible consistent moment error of up to ± 30 per cent due to uncertainties in the time function duration of about ± 1 sec. Note that this final moment determination is different from the preliminary value presented by Langston and Butler (1975).

Discussion

The focal mechanism of a north-south striking, westward dipping, normal dip-slip fault agrees perfectly with the configuration of the aftershock zone (Bufe *et al.*, 1976; Ryall and VanWormer, 1975). An estimate of 10×10 km for the fault plane area taken from the aftershock zone yields an average displacement of 17 cm on the fault. The shallow depth of 5.5 km also implies that rupture may have initiated near the center of the aftershock area and propagated radially outward. The time function duration of 3 sec and fault bounds assumed above yield a rupture velocity of less than 2 km/sec, assuming a simple propagating step dislocation model (Savage, 1966). These simple calculations indicate that the time function found here is adequate to explain the faulting process as indicated by the aftershock zone. Hart *et al.* (1975) found a moment of 1.9×10^{25} dyne-cm from teleseismic long-period surface waves. This discrepancy may lie in wave propagation phenomena, such as Q, affecting either estimate. Alternatively, slow slip occuring before or after the major fast movement is also a viable source model and would result in enhanced long-period moment estimates. Geodetic control could offer constraints on speculations such as these.

The possible 6.5-sec difference between the foreshock and mainshock origin times, seen in some short-period seismograms, versus 8.1 sec observed at short distance, has a simple explanation in terms of the focal mechanism. For regional stations ($\Delta \sim 150$ km) rays will be leaving the focal sphere toward the outer edge of the station distribution seen in Figure 1. This means that, in general, direct P is near a node. The small direct P, arriving within the foreshock wave train, could easily be missed and the large surface reflections picked instead as the first arrival.

Conclusions

From an analysis of P and S wave forms the mechanism of the mainshock of the Oroville earthquake sequence is determined to be dip 65°W, north-south strike, and rake $-70°$ (left-lateral). The far-field time function is modeled successfully as a symmetric triangular pulse 3 sec in duration. Scaling the amplitudes of the theoretical to the observed yields a moment of $5.7 \pm 2.0 \times 10^{24}$ dyne-cm. An additional ± 30 per cent maximum bias may exist in this moment determination due to uncertainties in the time function. The duration of the time function is consistent with the faulting area determined by the aftershock zone. A hypocentral depth determination of 5.5 ± 1.5 km is made using both the long- and short-period P waves. This focal mechanism is consistent with the configuration of the aftershock zone and the regional stress pattern.

Acknowledgments

We would like to thank the numerous seismic station administrators throughout the world who took their valuable time to respond to our seismogram requests. We also would like to extend our gratitude to Don Helmberger and Tom Heaton for their critical reviews of the manuscript. This research was supported by the Advanced Research Projects Agency of the Department of Defense and was monitored by the Air Force Office of Scientific Research under Contract F44620-72-C-0078. One of the authors (R.B.) was supported by the Fannie and John Hertz Foundation.

References

Bufe, C. G., F. W. Lester, K. M. Lahr, L. C. Seekins, and T. C. Hanks (1976). Oroville earthquakes: normal faulting in the Sierra Nevada foothills, submitted for publication.

Carpenter, E. W. (1966). Absorption of elastic waves—An operator for a constant Q mechanism, *AWRE Report 0-43/66*, H.M. Stationery Office.

Eaton, J. P. (1966). Crustal structure in northern and central California from seismic evidence, *Calif. Div. Mines and Geol. Bull.* **190,** 419–426.

Futterman, W. I. (1962). Dispersive body waves, *J. Geophys. Res.* **67,** 5279–5291.

Hart, R. S., R. Butler, and H. Kanamori (1975). Surface wave and ultra-long period body wave constraints on the August 1, 1975, Oroville earthquake, *Trans. Am. Geophys. Union* **56,** 1023.

Helmberger, D. V. and G. R. Engen (1974). Upper mantle shear structure, *J. Geophys. Res.* **79,** 4017–4028.

Langston, C. A. (1976). A body wave inversion of the Koyna, India, earthquake of 10 December 1967 and some implications for body wave focal mechanisms, *J. Geophys. Res.* (in press).

Langston, C. A. and D. V. Helmberger (1975). A procedure for modelling shallow dislocation sources, *Geophys. J.* **42,** 117–130.

Langston, C. A. and R. Butler (1975). Preliminary focal mechanism of the August 1, 1975, Oroville earthquake, *Trans. Am. Geophys. Union* **56,** 1023.

Mellman, G., L. Burdick, and D. Helmberger (1975). Determination of source parameters from body wave seismograms (abstract), *Earthquake Notes* **46,** 44.

Morrison, P., B. Stump, and R. Uhrhammer (1975). The Oroville earthquake sequence and its characteristics, *Trans. Am. Geophys. Union* **56,** 1023.

Ryall, A. and J. D. VanWormer (1975). Field study of the August, 1975, Oroville earthquake sequence, *Trans. Am. Geophys. Union* **56,** 1023.

Savage, J. C. (1966). Radiation from a realistic model of faulting, *Bull. Seism. Soc. Am.* **56,** 577–592.

Seismological Laboratory
California Institute of Technology
Pasadena, California 91125

Division of Geological and Planetary Sciences
California Institute of Technology
Contribution No. 2718

Manuscript received February 19, 1976